ADVANCED ELECTRONIC MATERIALS Open Access
www.advelectronicmat.de

Electrolyte Gated Synaptic Transistor based on an Ultra-Thin Film of $La_{0.7}Sr_{0.3}MnO_3$

*Alejandro López, Javier Tornos, Andrea Peralta, Isabel Barbero, Francisco Fernandez-Canizares, Gabriel Sanchez-Santolino, María Varela, Alberto Rivera, Julio Camarero, Carlos León, Jacobo Santamaría, and Miguel Romera**

Developing electronic devices capable of reproducing synaptic functionality is essential in the context of implementing fast, low-energy consumption neuromorphic computing systems. Hybrid ionic/electronic three-terminal synaptic transistors are promising as efficient artificial synapses since they can process information and learn simultaneously. In this work, an electrolyte-gated synaptic transistor is reported based on an ultra-thin epitaxial $La_{0.7}Sr_{0.3}MnO_3$ (LSMO) film, a half-metallic system close to a metal-insulator transition. The dynamic control of oxygen composition of the manganite ultra-thin film with voltage pulses applied through the gate terminal allows reversible modulation of its electronic properties in a non-volatile manner. The conductance modulation can be finely tuned with the amplitude, duration, and number of gating pulses, providing different alternatives to gradually update the synaptic weights. The transistor implements essential synaptic features such as excitatory postsynaptic potential, paired-pulse facilitation, long-term potentiation/depression of synaptic weights, and spike-time-dependent plasticity. These results constitute an important step toward the development of neuromorphic computing devices leveraging the tunable electronic properties of correlated oxides, and pave the way toward enhancing future device functionalities by exploiting the magnetic (spin) degree of freedom of the half metallic transistor channel.

1. Introduction

Hardware neural networks pose a promising path toward intelligent and adaptable computing at low energy cost.[1–3] Electronic devices able to emulate efficiently the functionality of synapses are essential elements for these networks. In fact, the human brain can learn to process information and identify patterns outperforming the most powerful computers mainly due to the ability of synapses to tune the strength of synaptic connections and process information simultaneously.[4,5] This functionality, known as synaptic plasticity,[6] is crucial in learning processes and provides an efficient way to process and store information out of the scope of traditional Von Neumann architectures in which memory and processing are physically separated.[7,8]

Within this context, it would be highly desirable for artificial synaptic elements to simultaneously exhibit non-volatile

A. López, J. Tornos, A. Peralta, I. Barbero, F. Fernandez-Canizares, G. Sanchez-Santolino, M. Varela, A. Rivera, C. León, J. Santamaría, M. Romera
GFMC
Dept. Física de Materiales
Facultad de Física
Universidad Complutense de Madrid
Madrid 28040, Spain
E-mail: miromera@ucm.es

The ORCID identification number(s) for the author(s) of this article can be found under https://doi.org/10.1002/aelm.202300007

DOI: 10.1002/aelm.202300007

A. López, J. Camarero
IMDEA Nanociencia
C/Faraday 9, Madrid 28049, Spain

J. Tornos, A. Rivera, C. León, J. Santamaría, M. Romera
Unidad Asociada UCM/CSIC
Laboratorio de Heteroestructuras con Aplicación en Espintrónica
Madrid 28049, Spain

F. Fernandez-Canizares, G. Sanchez-Santolino, M. Varela
Instituto Pluridisciplinar
Universidad Complutense de Madrid
Madrid 28040, Spain

J. Camarero
Departamento de Física de la Materia Condensada and Departamento de Física Aplicada
IFIMAC and Instituto Nicolás Cabrera
Universidad Autónoma de Madrid
Madrid 28049, Spain

memory, multi-state analogue resistance, and plasticity.[7–9] Memristor devices provide an interesting approach toward this aim. Their resistance state depends on the previous history of applied voltage or current,[10,11] and they can implement important synaptic features in a more efficient, simple, and compact way than pure CMOS alternatives.[12–16] However, they usually have two terminals, so they cannot transfer (process) information and learn (update synaptic weights) simultaneously, as biological synapses.[4,5] Instead, processing is inhibited during learning, limiting the device efficiency. As an alternative, hybrid ionic/electronic electrolyte gated three-terminal synaptic transistors[17–26] provide a promising way to perform signal transmission and learning simultaneously and thus to realize flexible synaptic operations efficiently. In fact, their working principle captures some of the most relevant features characteristic of the behavior of biological systems. In biological synapses the voltage-gated ion motion through ionic channels regulates the post-synaptic potential (i.e., the membrane potential of the post-synaptic neuron). Similarly, in electrolyte gated synaptic transistors the voltage-gated ion motion through an electrolyte regulates the potential (or the current) across the transistor channel, which plays the role of the postsynaptic terminal. In such systems, the conductance of the channel between source and drain represents the synaptic weight. Voltage pulses applied to the gate terminal, which can be seen as presynaptic spikes, create an electric double layer (EDL) at the channel interface. The EDL leads to a huge electric field that can give rise to electrochemical doping, via the insertion or extraction of ions such as H^+ or O^{2-} into or out of the channel. Electrochemical doping can be used to modify the channel conductance, emulating synaptic plasticity. Thus, information can be transmitted through the channel while synaptic weights can be modulated independently (and possibly simultaneously) through the gate.

Therefore, electrolyte gated transistors potentially offer ultra-low power operation,[20,21] highly linear modulation of synaptic weights[27] and good interfacing with biological environments due to their mixed ionic-electronic conductivity phenomena,[26] along with the possibility to realize programmable fluidic circuits.[17] Their operating mechanism, based on the creation of a defect diffusion profile at the channel through electrochemical doping, can be in principle better controlled than the stochastic formation of defects and filaments in resistive switching type memristors, potentially offering enhanced robustness to device-to-device and cycle-to-cycle variations.[27] The flexible gate structure of synaptic transistors allows the use of any number of gate electrodes as logic inputs on the electrolytes, emulating the connections of several pre-synaptic neurons[28] and forming parallel interconnected networks with reduced hardware connectivity.[29] Synaptic transistors constitute thus promising elements toward realizing efficient artificial synapses.

For such electrolyte gated synaptic transistors to work, materials whose conductivity can be modulated in a non-volatile manner via gate pulses applied through an electrolyte are required.[26] Synaptic transistors based on exchange of oxygen[30] are particularly attractive for applications since they are expected to exhibit longer retention properties and to be the simplest to integrate in stablished technologies when compared with other alternatives.[31,32] Although individual works with oxygen-based synaptic transistors have separately demonstrated some of the technical characteristics required for applications (1 V operating voltage,[33] 100 ns write lengths[34] and good on/off ratios[35]), there are not oxygen-based devices combining all these features together[32] and materials with optimal properties for reconfigurable analog computing are considered yet to be discovered.[31] This underlies the interest of investigating new promising materials for oxygen based synaptic transistors. Moreover, if those materials incorporate additional functionality to the synaptic behavior, new avenues may be opened toward the development of novel multifunctional devices with enhanced capabilities. Correlated oxides are good candidates for this aim since their electronic properties can be widely modified with different stimuli.[36,37] In particular, oxide thin films and interfaces can be drastically affected by the amount and profile of oxygen vacancies.[38–41] A prototypical example can be found in the $La_{1-x}Sr_xMnO_3$ system and, more specifically, in $La_{0.7}Sr_{0.3}MnO_3$ (LSMO), a half-metal with a perovskite structure characterized by a strong coupling between lattice, charge, and spin, providing a number of different degrees of freedom to externally manipulate its electronic properties including charge, orbital, spin, and magnetic ordering phenomena.[42–45] Thin LSMO films exhibit an insulator-metal transition whose transition temperature can be controlled with thickness,[46] strain,[47] and stoichiometry.[42,48] The electronic properties of planar LSMO structures have been shown to be affected by the profile[49] and amount[50] of oxygen vacancies within the structure, which can be modified combining in-plane electric fields[50] and joule heating.[49] Upon application of moderate voltages LSMO has shown to undergo reversible electrochemical reactions driven by displacement and ordering of oxygen vacancies[38,51] that may trigger phase changes from perovskite with octahedral Mn coordination to brownmillerite[52] with tetrahedral or pyramid Mn coordination. Moreover, reversible electronic and magnetic phase transitions induced by the creation/annihilation of oxygen vacancies via ionic liquid gating have been recently reported in LSMO compounds.[48,53] Adding the magnetoresistive nature of manganites to this electrolyte gated electronic transition, four non-volatile resistance states have been obtained by combining electric and magnetic fields.[53] These properties make LSMO interesting for a wide range of multifunctional memory devices and highlight its yet unexplored potential for synaptic devices.

In this work, we exploit the dynamic control of oxygen composition of an ultra-thin epitaxial LSMO film to report the first example of an LSMO based electrolyte-gated synaptic transistor. An ionic liquid (IL) connects the LSMO film with the gate electrode, which is used as the pre-synaptic terminal that controls the flow of ions toward the LSMO surface. This configuration, summarized in **Figure 1**, resembles the release of neurotransmitters in biological synapses and their control through pre-synaptic spikes. The LSMO channel is regarded as the postsynaptic terminal and its conductance as the synaptic weight. Positive gate pulses are used to progressively create oxygen vacancies in the LSMO channel modulating its electronic properties and leading to a multilevel non-volatile analogue resistance. We will show how this process is reversible, as the created oxygen vacancies can be annihilated with negative gate pulses. The electrolyte gated transistor implements essential synaptic features related to short-term and long-term memory and plasticity. These results are important toward the implementation of neuromorphic computing systems

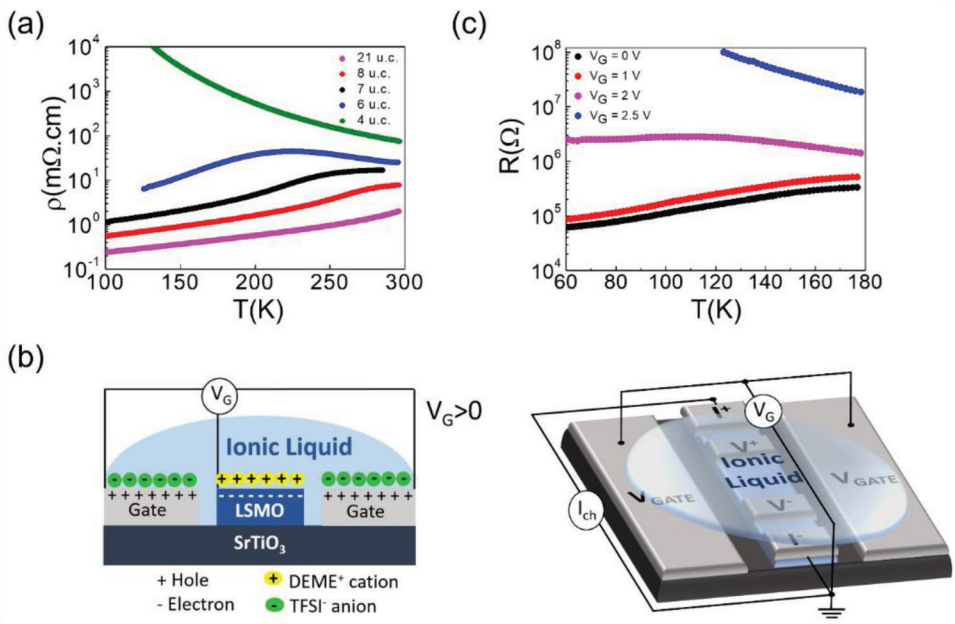

Figure 1. a) Temperature dependence of the resistivity of pristine LSMO films of different thicknesses. b) Schematics of the electrolyte gated transistor based on LSMO under positive gate voltage. Only electrostatic doping is considered (left). Top view of the device (right). c) Temperature dependence of the resistance of the LSMO channel in an electrolyte gated transistor after applying different gate voltages (see text). The nominal thickness of the LSMO channel is 6 u.c.

based on robust oxides and pave the way toward enhancing future device capabilities by exploiting the half-metallic character of the manganite transistor channel.

2. Results and Discussion

Epitaxial, high quality $La_{0.7}Sr_{0.3}MnO_3$ thin films were grown onto (001) oriented $SrTiO_3$ (STO) substrates at high temperatures (900 °C), using a high-pressure sputtering technique in pure oxygen atmosphere (see Experimental Section). Macroscopically averaged X-ray diffraction (Figure S1, Supporting Information) measurements indicate high crystalline quality. Figure 1a shows the resistivity–temperature (ρ–T) loop of pristine LSMO thin films of different thicknesses, exhibiting an insulator-metal transition with a transition temperature that increases with thickness. Electric double layer transistors in a side gating geometry were then fabricated (see schematics in Figure 1b and the Experimental Section for details). The ionic liquid *N*,*N*-diethyl-*N*-methyl(2-methoxyethyl) ammonium bis(trifluoromethylsulfonyl)imide ($[DEME]^+[TFSI]^-$) was chosen as electrolyte for its strong regulation ability,[48] high ionic conductivity, well known electrochemical properties,[54,55] and low glass transition temperature[54] ($T_C \approx 182$K) below which the mobility of ions becomes negligible.

First, we explore the ability to modulate the electronic properties of the LSMO channel by studying the evolution of the R–T characteristics with gate voltage (V_G). For this aim, a constant gate voltage is applied during 5 min at 230 K and while the device is cooled down below the glass transition temperature. V_G is then set to zero and R–T measurements are performed below T_C. Figure 1c shows the R–T curves after applying this procedure with different gate voltages to a sample with a nominal thickness of 6 unit cells (u.c.), which has an insulator-metal transition temperature slightly above T_C (Figure 1a). Figure 1c shows that a strong resistance modulation and a metal-insulator transition are induced in the LSMO channel upon increasing gate voltage.

It is important to note that the mechanism responsible for the modulation of the electronic properties shown in Figure 1c could have an electrostatic origin (electron doping),[37] an electrochemical origin (creation of oxygen vacancies),[53] or a combination of both. In fact, reversible electrochemical oxygen exchange between the ionic liquid (or its interface with the film) and the film has been demonstrated in the past in LSMO[53] and other oxide films.[56] The actual nature of charge carriers, and hence the underlying phenomenon, can be inferred from the analysis of the dynamic response of the LSMO channel resistance while it is modulated by gate voltage at a constant temperature above T_C (see **Figure 2**a). For this aim, a low constant current of $I_{ch} = 5$ μA is applied through the channel, so that the voltage across the channel remains more than an order of magnitude below the gate voltage. Likewise, the leakage current between the gate and the channel remains three orders of magnitude smaller than I_{ch}, ensuring that it does not affect device performance. Gating experiments are performed at 215 K to ensure ionic mobility within the ionic liquid and chemical stability in the LSMO surface. In all the electronic measurements shown from now on we use a LSMO film with a nominal thickness of 7 u.c., which has an insulator-metal transition temperature slightly above 215 K, therefore within the metallic regime (see Figure 1a). Figure 2a shows the R–V_G curve measured by sweeping gate voltage from 0 to 1.5 V, 1.5 to −2 V, and then back to 0 V at a rate of 5 mV s^{-1}. The channel resistance can be reversibly modulated toward higher or lower

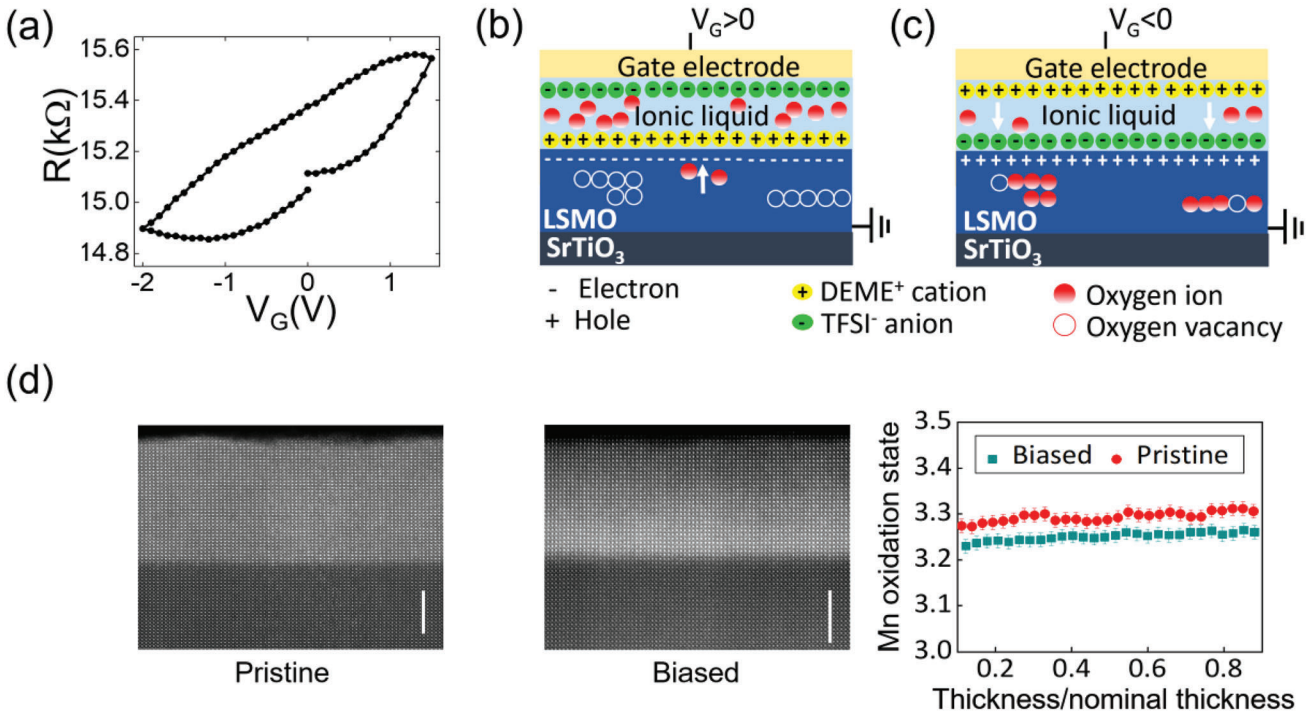

Figure 2. a) Resistance of the LSMO channel as a function of gate voltage (V_G) at 215 K. The sweeping rate was 5 mV s^{-1}. The curve was measured by sweeping gate voltage from 0 to 1.5 V, 1.5 to −2 V, and then back to 0 V. The source terminal (I^- in Figure 1b) was grounded during the sweep. The nominal thickness of the LSMO channel is 7 u.c. b) Schematic representation of the progressive creation of oxygen vacancies with positive gate voltages and c) their annihilation with negative gate voltage. d) STEM-EELS characterization of pristine and biased LSMO thin films. (Left) Atomic resolution Z-contrast STEM image of a 13.5 nm pristine LSMO thin film grown over STO (001) substrate. (Middle) Atomic resolution Z-contrast STEM image of a 11.5 nm biased LSMO thin film grown over STO (001) substrate. Scale bar in both images is 5 nm. (Right) Mn oxidation state profiles as a function of distance from the interface obtained from the O K edge fine structure analysis. To facilitate comparison between both layers, the thickness was normalized to the layer thickness. To avoid artefacts associated with surface damage and interfacial phenomena the profiles were taken in the normalized thickness range of 0.1–0.9.

values with positive and negative gate voltage respectively. On one hand, we note that the resistance measured while the maximum positive gate voltage (V_G = 1.5 V) is applied is larger than the resistance measured at V_G = 0 V, indicating a volatile electrostatic contribution. On the other hand, a hysteretic behavior is observed, evidencing that non-volatile electrochemical processes are also likely to be involved. In fact, this kind of hysteretic behavior in ionic liquid-gated LSMO has been reported[53] to be due to the progressive creation of oxygen vacancies in the LSMO film along with the ensuing reduction of Mn^{4+} to Mn^{3+} for positive gate voltages (Figure 2b), followed by the annihilation of oxygen vacancies and the consequent oxidation of Mn^{3+} back to Mn^{4+} for negative gate voltages (Figure 2c).

The effects of a non-volatile electrochemical doping were explored by scanning transmission electron microscopy and electron energy-loss spectroscopy (STEM-EELS) through the characterization of two LSMO films before (pristine) and after application of a gate voltage of V_G = 1.5 V for 2 h (see the Experimental Section for more details). Film thicknesses for this experiment were chosen in the 10–15 nm range to prevent the specimen preparation process for STEM observation from causing damage of ultra-thin films. Figure 2d shows two atomic resolution Z-contrast STEM images of both pristine (left) and biased (middle) LSMO thin films grown on a $SrTiO_3$ (001) substrate. The crystal structure quality is very high, interfaces appear sharp, epitaxial and free of major defects. 2D EEL spectrum images sampling lateral distances of tens of nm were acquired across the thickness of the layers to probe composition and electronic properties. In particular, EELS O *K* edge fine structure analysis was carried out to quantify the Mn oxidation state for both thin films, since the edge structure is directly related to the electronic structure, while the edge intensity is related to the O stoichiometry. For calibration we use the linear correlation between the difference in pre-peak and the adjacent main peak energies and Mn valence.[57] Values of the Mn oxidation state, averaged laterally over 15–20 nm, as a function of depth within the film all the way from the substrate interface to the surface are shown in Figure 2d (right). For the pristine film, the Mn oxidation state is quite even through the specimen thickness, with values close to the nominally expected +3.3 for a fully oxygenated $La_{0.7}Sr_{0.3}MnO_3$ system, with an average value of +3.294 ± 0.015. On the other hand, the film after biasing exhibits a homogeneous, slightly reduced Mn oxidation state values all through its thickness, with an average of +3.250 ± 0.015. Since no permanent electronic effect is expected to be derived from electrostatic doping, this reduction of the Mn oxidation state could be explained by a slight decrease of the local O content related to a process of electrochemical doping induced by the gating that results in a compositional change of the sample represented by the stoichiometric formula $La_{0.7}Sr_{0.3}MnO_{3-\delta}$, where δ accounts for the oxygen deficiency in the sample, i.e.,

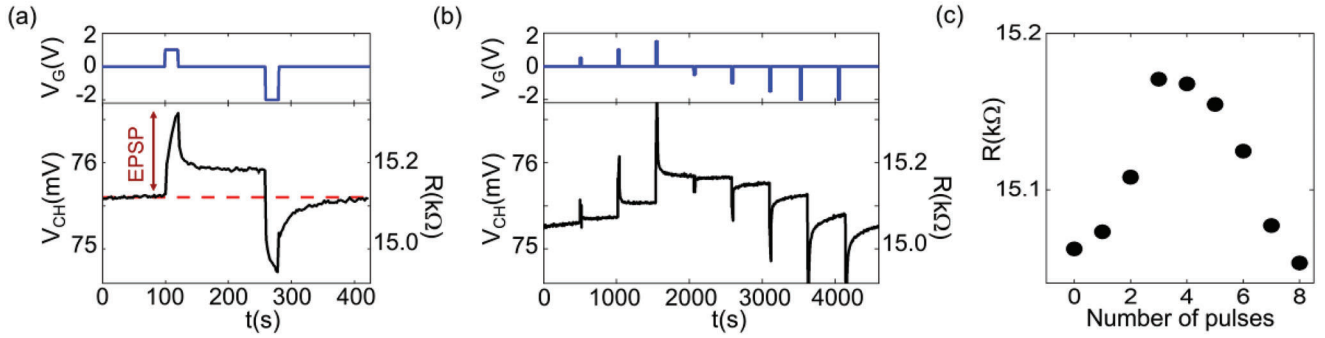

Figure 3. a,b) Temporal dependence of the voltage (left axis) and the resistance (right axis) across the LSMO channel (black line) upon applying a) a gate pulse of $V_G = 1$ V for 20 s followed by a gate pulse of $V_G = -2$ V for 20 s spaced 150 s apart (blue line), and b) a sequence of gate pulses of 0.5, 1, 1.5, −0.5, −1, −1.5, −2, and −2 V respectively, with a duration of 10 s and separated 500 s apart. A constant current of $I_{ch} = 5$ μA is applied through the channel. c) Resistance recorded 500 s after each pulse of the sequence. The nominal thickness of the LSMO channel is 7 u.c..

presence of oxygen vacancies (V_o). Assuming that each V_o dopes the material with up to 2 e^-, and that all changes in the Mn oxidation state after gating come from changes in O concentration, we can calculate the associated V_o concentration per unit cell (δ) in the biased sample from the experimental Mn oxidation state using expression (1) derived from charge neutrality.

$$\delta = \frac{3.3 - MnOxState}{2} \quad (1)$$

Introducing the average Mn oxidation state of the biased layer, the oxygen deficiency is found to be $\delta = 0.025 \pm 0.008$, meaning that the gating process has induced a density of O vacancies into the biased sample, changing this sample composition from $La_{0.7}Sr_{0.3}MnO_3$ to $La_{0.7}Sr_{0.3}MnO_{2.975}$. Interestingly, such compositional reduction would represent a shift in the phase diagram toward the metal to insulator boundary that separates the ferromagnetic metal from the insulator regions near a La/Sr composition x = 0.2.

The hysteretic behavior shown in Figure 2a is promising to implement synaptic functionality.[19,23] In order to confirm this potential, we study the temporal evolution of the voltage across the LSMO channel (V_{ch}) with a constant applied current of $I_{ch} = 5$ μA upon applying gate pulses, in analogy to the post-synaptic potential induced by pre-synaptic spikes in biological synapses.[4] **Figure 3**a shows V_{ch} as a function of time when a gating pulse of $V_G = +1$ V and a duration of 20 s is applied, followed by another pulse of $V_G = -2$ V and a duration of 20 s, separated 150 s apart. The first pulse triggers a potential enhancement in the LSMO channel (postsynaptic terminal) that closely resembles the excitatory postsynaptic potential (EPSP) observed in biological synapses.[4] An EPSP in neuroscience is a variation in the postsynaptic potential that makes the postsynaptic neuron more likely to fire. It is an essential synaptic feature caused by a gated influx of ions, which underlies the main process of information transmission between presynaptic and postsynaptic neurons. Figure 3a shows that the EPSP smoothly decays with time when the gate pulse is removed, resembling the forgetting curve of biological synapses, related to short-term memory. The decay of V_{ch} upon removing the gate pulse confirms that part of the voltage (resistance) enhancement is volatile and corresponds to electrostatic processes (electron doping). Interestingly, the initial resistance state is not totally recovered when the gate pulse is removed. Instead, a non-volatile enhancement of the channel resistance due to the creation of oxygen vacancies in the LSMO layer with positive gate pulses (Figure 2b) and related to long-term memory is observed. Importantly, the non-volatile resistance variation is reversible and the initial state can be recovered (the created oxygen vacancies can be annihilated, Figure 2c) by applying a gate pulse of opposite polarity (Figure 3a). The coexistence of short-term potentiation and long-term memory states occurs in biological memories and allows merging processing and storage capabilities in a single device.[26]

Figure 3a shows that bi-stable resistance states can be controlled by applying pulses of opposite polarity. This finding is important because emulating synaptic functionality requires the ability to access multi-level analogue-like resistance states in a reversible manner. To investigate if the synaptic transistor implements this functionality, we monitor the device resistance while a train of pulses of different amplitudes and polarities is applied (Figure 3b). The resistance recorded 500 s after each pulse is shown in Figure 3c and confirms that several non-volatile resistance states can be obtained in a reversible manner. Figure 3b,c suggest that the amplitude of the EPSP (the maximum volatile value of V_{ch}) as well as the non-volatile variation of the resistance depends on the amplitude of the applied pulse. Indeed, the first pulse of 0.5 V induces a mainly volatile response and the non-volatile variation of the resistance increases with gate voltage. To investigate this behavior in detail, we study the temporal response of V_{ch} and the resistance to single gate pulses of different characteristics, as summarized in **Figure 4**. First, gate pulses of different duration and identical amplitude are applied. Figure 4a shows that both the amplitude of the EPSP and the final non-volatile resistance can be finely tuned with the duration of the gate pulse. Figure 4d displays the amplitude of the EPSP (green symbols) and the non-volatile change of resistance (red symbols) as a function of pulse duration, which follows a linear dependence. Then, we apply gate pulses of the same duration and different amplitude. Figure 4b shows that the EPSP and the non-volatile channel resistance can also be gradually tuned with the amplitude of the gate pulse. Figure 4e summarizes the volatile and non-volatile variation of V_{ch} as a function of gate amplitude, which follows an exponential dependence. Finally, we study the temporal evolution of V_{ch} while sequences with a

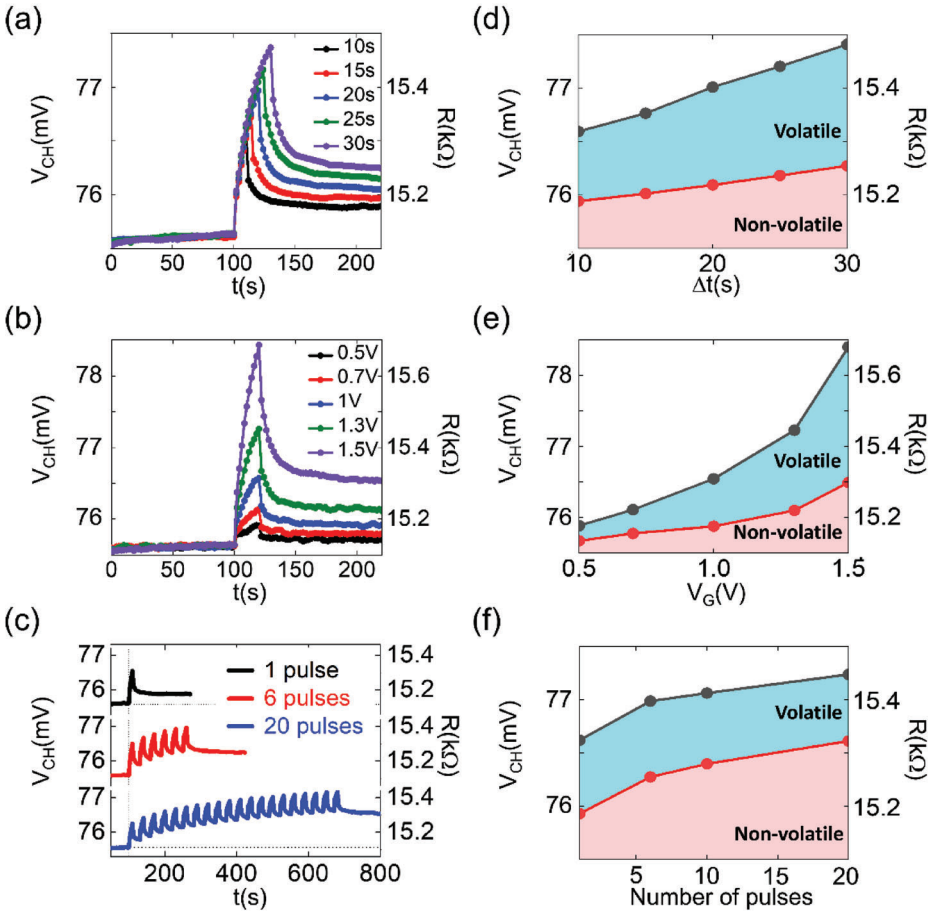

Figure 4. a–c) Time evolution of the voltage (left axis) and the resistance (right axis) across the LSMO channel upon applying a) single gate pulses of V_G = 1 V and different durations, b) single gate pulses of different amplitude and a duration of 20 s and c) sequences of one (black curve), six (red curve), and twenty (blue curve) identical gate pulses of 1 V and a duration of 10 s separated 20 s apart. The curves are shifted for clarity. d–f) Volatile and non-volatile variation of the voltage across the LSMO channel (resistance) as a function of d) pulse duration, e) gate voltage and f) number of pulses. A constant current of I_{ch} = 5 μA is applied through the channel. The initial resistance state was reset between measurements.

different number of identical pulses are applied (Figure 4c). A gradual increase of the volatile (EPSP) and non-volatile variation of the LSMO channel resistance is obtained with the number of pulses (Figure 4f).

The possibility to gradually tune the EPSP and the non-volatile variation of the resistance in an analogue way with the duration, amplitude, and number of gating pulses provides different alternatives to finely control the synaptic weights. Note that the initial resistance state is identical in all the measurements of Figure 4. For this, a gate voltage of $V_G = -2$ V is applied to the gate terminal after each measurement until the initial resistance state of the channel is recovered, underlying the reversibility of the processes involved.

The ability to modulate the strength of synaptic connections with gating pulses provides an opportunity to implement synaptic plasticity, an essential functionality to emulate the learning and memory functions of biological systems. Plasticity can be divided into short-term plasticity and long-term plasticity depending on the time scale at which resistance variations are maintained. A synaptic property related to short-term activity dependent plasticity that is crucial to decode temporal information in visual or auditory systems is paired-pulse facilitation (PPF).[4,58] It is the property by which, when a biological synapsis receives consecutives presynaptic spikes in a short period of time, the excitatory postsynaptic potential induced by the second spike ($EPSP_2$) is well above the one induced by the first spike ($EPSP_1$).[19,22,28] The relative enhancement of the second excitatory postsynaptic potential (PPF = $EPSP_2/EPSP_1$) is directly related to the time interval between spikes: the closer the paired spikes arrive the larger the relative enhancement of the postsynaptic potential. **Figure 5** shows that our synaptic device successfully implements PPF. When it receives two input pulses separated by a large time interval, both pulses induce a similar postsynaptic potential (Figure 5a, PPF = 1.1). In contrast, if the two input pulses are separated by a short time interval, the second pulse induces a postsynaptic potential that is well above the one induced by the first pulse (Figure 5b, PPF = 1.35). To further investigate the influence of the time interval between pulses in the PPF behavior, we measure the device response to pairs of pulses with different time delays. Figure 5c shows that the PPF index decreases from 1.7 to 1.1 as the time interval between consecutive pulses increases from 5 to 100 s. As in biological

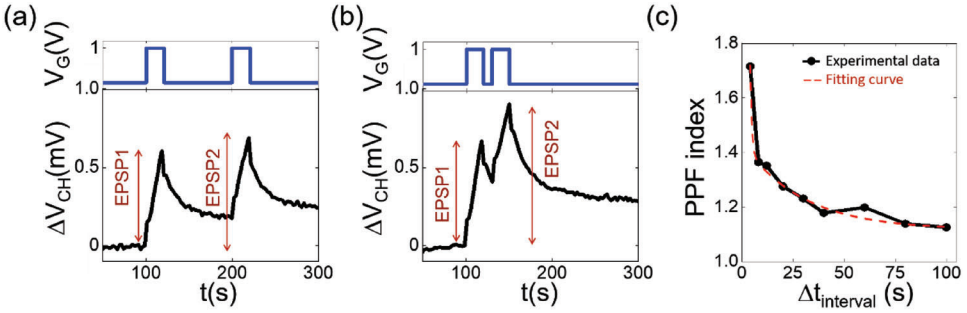

Figure 5. a,b) Temporal evolution of the voltage variation across the LSMO channel (V_{ch}(t)-V_{ch}(0)) when a pair of identical pulses of V_G = 1 V and a duration of 20 s separated a) 80 s and b) 10 s is applied. c) Pair pulse facilitation index (PPF = $EPSP_2/EPSP_1$) as a function of the time interval between pulses fitted with a double exponential function (see text). The initial resistance state was reset between measurements.

synapses,[59] the dependence of the PPF index with the time interval can be described with a double exponential function PPF = 1 + $C_1 \cdot \exp(-\Delta t/\tau_1)$ + $C_2 \cdot \exp(-\Delta t/\tau_2)$, where Δt is the time interval between pulses, C_1 and C_2 are the initial facilitation magnitudes, and τ_1 and τ_2 are the characteristic relaxation times.[19,22,28,59] It is possible to fit our data to such model with values of C_1 = 309.5, C_2 = 0.33, τ_1 = 0.7 s and τ_2 = 28.9 s, as shown in Figure 5c. The characteristic relaxation times are of the order of seconds at this temperature, which is around one order of magnitude larger than those of biological synapses.[59] The PPF behavior and the time scale of the characteristic relaxation times can be explained as follows. The PPF effect is related to short-term memory, which in our device corresponds to electrostatic effects and can be explained in terms of the ionic relaxation within the ionic liquid (and the associated relaxation of electrostatic doping inside the manganite) between the first and the second pulse. When the time interval between two input pulses is short, ions in the ionic liquid do not have time to relax away from the LSMO surface between the first and the second pulse. Therefore, the second pulse gives rise to a larger charge accumulation at the LSMO surface than the first pulse. In contrast, if the time interval is larger than the ionic relaxation time, the second pulse arrives once most of the ions in the ionic liquid have relaxed away from the LSMO surface (which is close to the pristine state) so it induces a similar response than the first pulse. At this temperature, ions in the ionic liquid are mobile enough to induce the effect in the LSMO film in a time scale of seconds. This defines the time scale of the device short-term memory (i.e., the characteristic relaxation times τ_1 and τ_2) and the speed of the resistance modulation induced with gating. The speed of the synaptic device is thus expected to increase exponentially with temperature, as the ionic liquid mobility.[54] This is discussed in more detail later on. The PPF behavior and the ionic mechanism involved are analogous to the control mechanism of neurotransmitters in biological synapses[59] and evidence that the synaptic transistor can implement short-term memory functions.

Another important synaptic property is long-term plasticity,[6,60] which is responsible for long-term memory and learning. It consists in a persistent increase (long-term potentiation) or decrease (long-term depression) of the synaptic weights, represented here by the channel conductance. Long-term plasticity is investigated by monitoring the response of the non-volatile resistance to a sequence of 20 identical gate pulses of positive polarity (V_G = 1 V for 10 s), followed by 20 identical gate pulses of negative polarity (V_G = −2 V for 10 s). Resistance is recorded 500 s after each pulse. Figure 6a shows the evolution of long-term plasticity with the number of pulses. An increasing number of positive pulses gradually increases the amount of oxygen vacancies in the LSMO film, translating into an enhancement of the resistance (synaptic depression). By applying 20 pulses of negative polarity oxygen vacancies are progressively annihilated and the resistance is gradually reduced (synaptic potentiation) until the initial resistance state is roughly recovered. The potentiation and depression rates can be tuned with the duration and amplitude of input pulses (Figure 3). **Figure 6**a exhibits an almost linear depression, as desired in synaptic elements, but potentiation is unfortunately not linear. Non-linear and asymmetric potentiation-depression are commonly observed in synaptic devices.[61] Linearity and symmetry can be improved by optimizing the scheme of programming pulses, either relying on shorter identical pulses of larger amplitude[62] or using pulses with incremental amplitude or pulse width.[61,63] Alternatively, linearity of the channel conductance as a function of the number of pulses is strongly related to the ionic conductivity of the electrolyte and can be improved for instance by using optimized solid-state electrolytes.[33,64]

The potentiation-depression curve of Figure 6a exhibits at least 20 different non-volatile resistance states. Retention data of different resistance states is shown in Figure S2 (Supporting Information). These results evidence that the device implements analogue-like multistate behavior and long-term plasticity.

Several mechanisms have been proposed[60] to explain how the human brain learns by reconfiguring the strength of synaptic weights, without any previous knowledge of the processed information.[65] A particularly interesting mechanism is spike-time-dependent plasticity[66] (STDP), which proposes that synaptic weights are modified depending on the causal relation and time difference between presynaptic and postsynaptic spikes.[67] The most common way of STDP is asymmetric STDP[12,22] in which the presynaptic spike preceding the postsynaptic spike translates into the long-term potentiation of the synaptic weight, while pulses with the opposite order translate into long-term synaptic depression. In both cases, the shorter the time between pulses, the larger the variation of synaptic weights. STDP do not require previous information of the input data neither external control of the synaptic weights, so it is promising to implement self-learning (also known as unsupervised learning).[68] Asymmetric STDP can be implemented by connecting the presynaptic

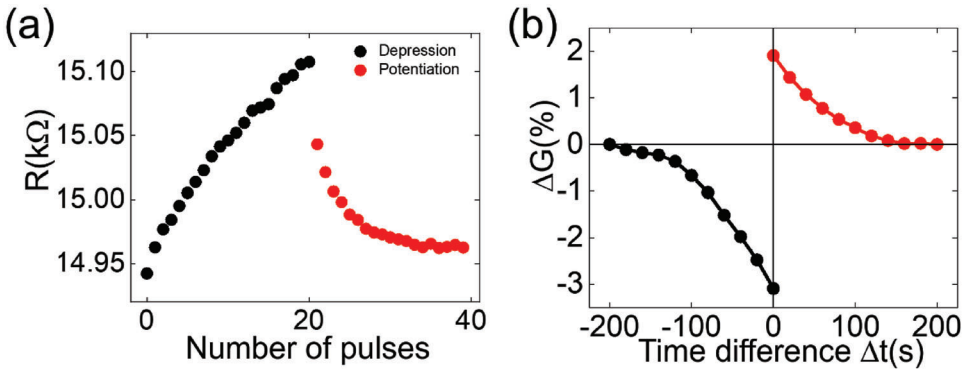

Figure 6. Long term potentiation and depression of synaptic weights and spike-time-dependent plasticity (STDP). a) Gradual modulation of the long-term resistance under 20 positive and 20 negative gate pulses (V_G = 1 V and V_G = −2 V respectively, for 10 s spaced 500 s apart), as a function of the number of pulses. Resistance was recorded 500 s after each pulse. b) Spike-time-dependent plasticity. Relative increase (potentiation) or decrease (depression) of synaptic weights as a function if the time interval between presynaptic and postsynaptic pulses Δt. The synaptic weight is represented by the channel conductance (G).

and postsynaptic terminals of the synaptic device to a multiplexer that converts the time difference between presynaptic and postsynaptic spikes in the amplitude of a voltage pulse.[69] The circuit required can be found in Figure S3 and Table S1 (Supporting Information). Here, we simulate the output of the multiplexer[17,22] by applying single gating pulses with a duration of 20 s whose amplitude and polarity parameterize the time difference between presynaptic and postsynaptic spikes (see Experimental Section and Note S1, Supporting Information). Figure 6b shows the measured percentage change of the channel conductance as a function of the simulated time difference. Long-term potentiation and depression are obtained for positive and negative time differences respectively, and the smaller the time difference the larger the resistance modulation. Such behavior can be fitted to an exponential decay function which is characteristic of the asymmetric STDP learning rule, thus emulating the long-term plasticity of biological synapses. The successful implementation of long-term potentiation, long-term depression and STDP with a manganite based synaptic transistor constitutes a step forward in the development of synaptic devices with long-term plasticity based on correlated oxides.

These results evidence that the proposed device based on oxygen exchange in an ultra-thin epitaxial LSMO film implements synaptic behavior. The device properties can be largely improved for its use in neuromorphic networks. The resistance variation can be enhanced by engineering the metal-insulator transition temperature of the LSMO ultra-thin film through further optimizing its thickness. Figure S4 (Supporting Information) shows a volatile and a non-volatile variation of the resistance of 90% and 45% respectively obtained with V_G = 2 V in a device based on a LSMO film with a nominal thickness between 6 and 7 u.c.. We note that larger resistance variations have been achieved by oxygen-based three terminal synaptic devices, often relying on high electric fields[35] and/or high temperatures.[70,30,31] Indeed, the resistance change in our device increases exponentially with gate voltage (see Figure 4e), which can be increased up to ± 4 V and above without any degradation of the ionic liquid.[56] Reducing the channel size, optimizing geometry, and using solid-state ionic conductors with high ionic mobility can also enhance the resistance change by several orders of magnitude[17] in future LSMO based devices.

Another important aspect for neuromorphic applications is the device speed, i.e., the time scale of programming pulses and the characteristic relaxation times. In our device, speed is defined by the ionic mobility within the ionic liquid and thus it is expected to increase exponentially with temperature, as the ionic mobility. We note that the results shown here can potentially be reproduced at RT and above by using an ionic liquid with higher glass transition temperature and a LSMO film with an insulator-metal transition temperature slightly above RT[71] (Figure 1a). This can speed up the LSMO based transistor by orders of magnitude. In addition, the speed of the device can also be largely enhanced by optimizing device geometry (reducing gate-channel distance and/or using top-gates)[17] or using fast solid-state electrolyte materials in thin films.[72] Indeed, fast solid-state ionic conductors such as yttria-stabilized zirconia (YSZ) can be grown epitaxially on top of (or under) LSMO.[73] Cyclability and device-to-device variations are also important aspects of synaptic elements. Different devices exhibit the same qualitative behavior, although their resistance values can change due to thickness variations between different deposited samples. This can be largely improved upon reducing device size so that different devices can be fabricated in the same sample. The LSMO-based transistor exhibits fairly good cycle-to-cycle variations (see Figure S5, Supporting Information). The future implementation of these devices in neuromorphic networks will require a detailed analysis of their coulombic efficiency [74] evolution with the number of cycles.

Finally, LSMO is a robust epitaxial oxide that enables high temperature operation and can be integrated on Silicon[75] and with other epitaxial oxides such as ferroelectric materials. In the future, device capabilities could be enhanced by exploiting the magnetic (spin) degree of freedom of the half-metallic ferromagnetic channel. Since the current flowing through the channel is highly spin polarized, this device offers, on one hand, a precise (analog) gate control of the spin polarized current injected in an adjacent system. This could be exploited in artificial neuronal networks based on spintronic neuron elements that communicate through spin polarized currents,[76] and

in spintronic applications that require an external analogue control of spin injection. On the other hand, the conductance of the LSMO channel is expected to change upon applying a magnetic field, [53] given the magneto-resistive nature of manganites. Tuning synaptic weights with magnetic fields, i.e., without the need of accessing the synapses electrically, could be a potential route toward enhancing endurance in future synaptic elements.

3. Conclusion

In summary, we have shown that the electronic properties of ultra-thin epitaxial LSMO films can be cumulatively modulated via electrolyte gating as required for synaptic transistors. We exploit the dynamic control of oxygen composition in the LSMO film to report multi-level non-volatile resistance states that can be controlled in an analogue and reversible manner through gate pulses. Different alternatives to finely tune the conductance of the LSMO channel with the amplitude, duration, and number of applied pulses have been discussed. The coexistence of non-volatile and volatile mechanisms in the synaptic transistor allows merging short-term and long-term memory functions and implementing important synaptic features such as excitatory postsynaptic potential, pair pulse facilitation, long-term potentiation/depression of synaptic weights and spike time dependent plasticity. This work constitutes a step forward in the development of neuromorphic computing devices based on strongly correlated manganites.

4. Experimental Section

Sample Preparation: Epitaxial $La_{0.7}Sr_{0.3}MnO_3$ thin films with different thickness ranging from 4 to 35 u.c. were grown onto (001) oriented SrTiO3 (STO) substrates at high temperatures (900 °C), in a high pressure (3.2 mbar) sputtering in pure oxygen atmosphere. Growth was followed by a 1 h annealing at 900 °C in pure oxygen (1 atm). X-ray diffraction and scanning transmission electron microscopy measurements have been used to confirm high epitaxial quality.

Device Fabrication: The $La_{0.7}Sr_{0.3}MnO_3$ thin films were patterned into a millimeter-scale channel with coplanar gate electrodes using standard photolithography techniques. The channel size was 1 mm times 5 mm. Ag electrodes with micrometer scale thickness were deposited via thermal evaporation. A drop of ionic liquid DEME-TFSI was deposited on the sample to serve as the electrolyte-gating medium, connecting the channel and the gate electrode. To prevent the reaction of the surface of the sample with water in the IL, the DEME-TFSI was baked at 100 °C and at 10^{-2} torr for a period of 24 h.

Electrical Measurements: The LSMO electrical characteristics were measured using a Keithley 2400 in a closed cycle He cryostat. Gating was applied using a Keithley 2611b. To obtain the STDP curve, the device was initialized after each measurement to the state of high resistance for $\Delta t < 0$ by applying $V_G = 1$ V during 30 s, and to a low resistance state for $\Delta t > 0$ by applying $V_G = -2$ V during 30 s. Conductance was measured 100 s after each pulse. STDP measurements were performed at 230 K.

STEM-EELS Characterization: For STEM-EELS observation, cross-section LSMO thin film specimens were prepared by conventional mechanical grinding and polishing and Ar ion milling. Two samples were analyzed: 1) a 13.5 nm pristine LSMO layer and 2) a 11.5 nm layer after application of $V_G = 1.5$ V during 2 h (biased film). Specimens were characterized using an aberration-corrected JEOL JEM-ARM 200cF electron microscope operated at 200 kV and equipped with a cold field emission gun and a Gatan Quantum electron energy loss spectrometer. For spectrum imaging, the electron beam was scanned along a 2D region of interest and an EEL spectrum image was acquired with a sampling of one unit cell per pixel and an exposure time of 0.1 s/pixel, enabling a 16 sub-pixel scan to average the spectrum over the complete unit cell. Mn oxidation state was calculated by fitting the O *K* edge pre-peak and second peak to a Gaussian curve. Mn oxidation states were extracted as a function of energy separation (calculated as the difference between positions of the second peak and the pre-peak) for every pixel in the EELS spectrum image.[57] The profiles in Figure 2d were obtained by averaging the 2D EEL spectrum images along the direction parallel to the interface. To facilitate comparison between both layers and to avoid effects associated with surface damage, the thickness was normalized to the layer thickness and profiles were taken in the normalized thickness range of 0.1–0.9.

Supporting Information

Supporting Information is available from the Wiley Online Library or from the author.

Acknowledgements

This work was supported by the Spanish MCI, AEI and FEDER under Grant Nos. PID2020-116181RB-C33, PID2020-116181RB-C31 and PGC2018-099422-A-I00 (MCI/AEI/FEDER, UE) and by Comunidad de Madrid under Grant Nos. S2018/NMT-4321 (NanomagCOST-CM) and 2018-T1/IND-11935 (Atracción de Talento). A.L. was funded through the FPU Fellowship No. FPU20/02408. IMDEA-Nanociencia acknowledges support from the "Severo Ochoa" Program for Centers of Excellence in R&D (CEX2020-001039-S). F.F.-C. and M.V acknowledge financial support from Spanish MICINN PID2021-122980OB-C51 (MCI/AEI/FEDER/UE). G.S.-S. acknowledges financial support from Spanish MCI Grant Nos. RTI2018-099054-J-I00 (MCI/AEI/FEDER, UE) and IJC2018-038164-I. Electron microscopy observations were carried out at the Centro Nacional de Microscopia Electronica, CNME-UCM.

Conflict of Interest

The authors declare no conflict of interest.

Data Availability Statement

The data that support the findings of this study are available from the corresponding author upon reasonable request.

Keywords

artificial synapses, electrolyte gating, manganite oxide films, synaptic transistors

Received: January 4, 2023
Revised: March 15, 2023
Published online:

[1] P. A. Merolla, J. V. Arthur, R. Alvarez-icaza, A. S. Cassidy, J. Sawada, F. Akopyan, B. L. Jackson, N. Imam, C. Guo, Y. Nakamura, B. Brezzo, I. Vo, S. K. Esser, R. Appuswamy, B. Taba, A. Amir, M. D. Flickner, W. P. Risk, R. Manohar, D. S. Modha, *Science* **2014**, *345*, 668.
[2] G. Indiveri, S. C. Liu, *Proc IEEE Inst Electr Electron Eng* **2015**, *103*, 1379.

[3] D. Querlioz, O. Bichler, A. F. Vincent, C. Gamrat, *Proc IEEE Inst Electr Electron Eng* **2015**, *103*, 1398.
[4] M. W. Halterman, *Neuroscience*, 3rd ed., **2005**.
[5] E. R. Kandel, *Science* **2015**, *294*, 1030.
[6] D. O. Hebb, *Wiley: New York* **1949**.
[7] D. Kuzum, S. Yu, H.-S. P. Wong, *Nanotechnology* **2013**, *24*, 382001.
[8] J. Del Valle, J. G. Ramírez, M. J. Rozenberg, I. K. Schuller, *J. Appl. Phys.* **2018**, *124*, 211101.
[9] D. Seok Jeong, I. Kim, M. Ziegler, H. Kohlstedt, *RSC Adv.* **2013**, *3*, 3169.
[10] L. Chua, *IEEE Transactions on Circuit Theory* **1971**, *18*, 507.
[11] J. J. Yang, D. B. Strukov, D. R. Stewart, *Nat. Nanotechnol.* **2013**, *8*, 13.
[12] S. H. Jo, T. Chang, I. Ebong, B. B. Bhadviya, P. Mazumder, W. Lu, *Nano Lett.* **2010**, *10*, 1297.
[13] Z. Wang, S. Joshi, S. E. Savel'ev, H. Jiang, R. Midya, P. Lin, M. Hu, N. Ge, J. P. Strachan, Z. Li, Q. Wu, M. Barnell, G.-L. Li, H. L. Xin, R. S. Williams, Q. Xia, J. J. Yang, *Nat. Mater.* **2017**, *16*, 101.
[14] A. Serb, J. Bill, A. Khiat, R. Berdan, R. Legenstein, T. Prodromakis, *Nat. Commun.* **2016**, *7*, 12611.
[15] R. Berdan, E. Vasilaki, A. Khiat, G. Indiveri, A. Serb, T. Prodromakis, *Sci. Rep.* **2016**, *6*, 18639.
[16] M. A. Zidan, J. P. Strachan, W. D. Lu, *Nat. Electron.* **2018**, *1*, 22.
[17] J. Shi, S. D. Ha, Y. Zhou, F. Schoofs, S. Ramanathan, *Nat. Commun.* **2013**, *4*, 2676.
[18] L. Q. Zhu, C. J. Wan, L. Q. Guo, Y. Shi, Q. Wan, *Nat. Commun.* **2014**, *5*, 3158.
[19] C. Sen Yang, D. S. Shang, N. Liu, G. Shi, X. Shen, R. C. Yu, Y. Q. Li, Y. Sun, *Adv. Mater.* **2017**, *29*, 1700906.
[20] Y. van de Burgt, E. Lubberman, E. J. Fuller, S. T. Keene, G. C. Faria, S. Agarwal, M. J. Marinella, A. Alec Talin, A. Salleo, *Nat. Mater.* **2017**, *16*, 414.
[21] W. Xu, S.-Y. Min, H. Hwang, T.-W. Lee, *Sci. Adv.* **2016**, *2*, 1501326.
[22] J. T. Yang, C. Ge, J. Y. Du, H. Y. Huang, M. He, C. Wang, H. Bin Lu, G. Z. Yang, K. J. Jin, *Adv. Mater.* **2018**, *30*, 1801548.
[23] C. Ge, C. xiang Liu, Q. li Zhou, Q. hua Zhang, J. yu Du, J. kun Li, C. Wang, L. Gu, G. zhen Yang, K. juan Jin, *Adv. Mater.* **2019**, *31*, 1900379.
[24] J. Zhu, Y. Yang, R. Jia, Z. Liang, W. Zhu, Z. U. Rehman, L. Bao, X. Zhang, Y. Cai, L. Song, R. Huang, *Adv. Mater.* **2018**, *30*, 1800195.
[25] E. J. Fuller, F. El Gabaly, F. Léonard, S. Agarwal, S. J. Plimpton, R. B. Jacobs-Gedrim, C. D. James, M. J. Marinella, A. A. Talin, *Adv. Mater.* **2017**, *29*, 1604310.
[26] H. Ling, D. A. Koutsouras, S. Kazemzadeh, Y. Van De Burgt, F. Yan, P. Gkoupidenis, *Appl. Phys. Rev.* **2020**, *7*, 011307.
[27] C. Yoon, G. Oh, B. H. Park, *Nanomaterials* **2022**, *12*, 1728.
[28] Y. H. Liu, L. Q. Zhu, P. Feng, Y. Shi, Q. Wan, *Adv. Mater.* **2015**, *27*, 5599.
[29] P. Gkoupidenis, D. A. Koutsouras, G. G. Malliaras, *Nat. Commun.* **2017**, *8*, 15448.
[30] H. Y. Huang, C. Ge, Q. H. Zhang, C. X. Liu, J. Y. Du, J. K. Li, C. Wang, L. Gu, G. Z. Yang, K. J. Jin, *Adv. Funct. Mater.* **2019**, *29*,1902702.
[31] A. A. Talin, Y. Li, D. A. Robinson, E. J. Fuller, S. Kumar, *Adv. Mater.* **2022**, 2204771.
[32] M. Huang, M. Schwacke, M. Onen, J. del Alamo, J. Li, B. Yildiz, *Adv. Mater.* **2023**, 2205169.
[33] R. D. Nikam, M. Kwak, H. Hwang, *Adv. Electron. Mater.* **2021**, *7*, 2100142.
[34] S. Kim, T. Todorov, M. Onen, T. Gokmen, D. Bishop, P. Solomon, K.-T. Lee, M. Copel, D. B. Farmer, J. A. Ott, T. Ando, H. Miyazoe, V. Narayanan, J. Rozen, in *2019 IEEE International Electron Devices Meeting (IEDM)*, **2019**, pp. 35.7.1–35.7.4.
[35] H. Kwak, C. Lee, C. Lee, K. Noh, S. Kim, *Semicond. Sci. Technol.* **2021**, *36*, 114002.
[36] Y. Tokura, M. Kawasaki, N. Nagaosa, *Nat. Phys.* **2017**, *13*, 1056.
[37] S. Hurand, A. Jouan, C. Feuillet-Palma, G. Singh, J. Biscaras, E. Lesne, N. Reyren, A. Barthélémy, M. Bibes, J. E. Villegas, C. Ulysse, X. Lafosse, M. Pannetier-Lecoeur, S. Caprara, M. Grilli, J. Lesueur, N. Bergeal, *Sci. Rep.* **2015**, *5*, 12751.
[38] P. Nukala, M. Ahmadi, Y. Wei, S. de Graaf, E. Stylianidis, T. Chakrabortty, S. Matzen, H. W. Zandbergen, A. Björling, D. Mannix, D. Carbone, B. Kooi, B. Noheda, *Science* **2021**, *372*, 630.
[39] V. Rouco, R. El Hage, A. Sander, J. Grandal, K. Seurre, X. Palermo, J. Briatico, S. Collin, J. Trastoy, K. Bouzehouane, A. I. Buzdin, G. Singh, N. Bergeal, C. Feuillet-Palma, J. Lesueur, C. Leon, M. Varela, J. Santamaría, J. E. Villegas, *Nat. Commun.* **2020**, *11*, 658.
[40] D. Hernandez-Martin, F. Gallego, J. Tornos, V. Rouco, J. I. Beltran, C. Munuera, D. Sanchez-Manzano, M. Cabero, F. Cuellar, D. Arias, G. Sanchez-Santolino, F. J. Mompean, M. Garcia-Hernandez, A. Rivera-Calzada, S. J. Pennycook, M. Varela, M. C. Muñoz, Z. Sefrioui, C. Leon, J. Santamaria, *Phys. Rev. Lett.* **2020**, *125*, 266802.
[41] V. Rouco, F. Gallego, D. Hernandez-Martin, D. Sanchez-Manzano, J. Tornos, J. I. Beltran, M. Cabero, F. Cuellar, D. Arias, G. Sanchez-Santolino, F. J. Mompean, M. Garcia-Hernandez, A. Rivera-Calzada, M. Varela, M. C. Muñoz, C. Leon, Z. Sefrioui, J. Santamaria, *APL Mater.* **2021**, *9*, 031110.
[42] Y. Tokura, *Rep. Prog. Phys.* **2006**, *69*, 797.
[43] A. Urushibara, Y. Moritomo, T. Arima, A. Asamitsu, G. Kido, Y. Tokura, *Phys. Rev. B* **1995**, *51*, 14103.
[44] J. Sakai, N. Ito, S. Imai, *J. Appl. Phys.* **2006**, *99*, 08Q318.
[45] D. Preziosi, M. Alexe, D. Hesse, M. Salluzzo, *Phys. Rev. Lett.* **2015**, *115*, 157401.
[46] Z. Liao, F. Li, P. Gao, L. Li, J. Guo, X. Pan, R. Jin, E. W. Plummer, J. Zhang, *Phys. Rev. B* **2015**, *92*, 125123.
[47] Y. Konishi, Z. Fang, M. Izumi, T. Manako, M. Kasai, H. Kuwahara, M. Kawasaki, K. Terakura, Y. Tokura, *J. Phys. Soc. Jpn.* **1999**, *68*, 3790.
[48] C. Ge, K. J. Jin, L. Gu, L. C. Peng, Y. S. Hu, H. Z. Guo, H. F. Shi, J. K. Li, J. O. Wang, X. X. Guo, C. Wang, M. He, H. Bin Lu, G. Z. Yang, *Adv. Mater. Interfaces* **2015**, *2*, 1500407.
[49] N. Manca, L. Pellegrino, D. Marré, *Appl. Phys. Lett.* **2015**, *106*, 203502.
[50] J. C. Gonzalez-Rosillo, R. Ortega-Hernandez, B. Arndt, M. Coll, R. Dittmann, X. Obradors, A. Palau, J. Suñe, T. Puig, *Adv. Electron. Mater.* **2019**, *5*, 1800629.
[51] L. Yao, S. Inkinen, S. van Dijken, *Nat. Commun.* **2017**, *8*, 14544.
[52] L. Cao, O. Petracic, P. Zakalek, A. Weber, U. Rücker, J. Schubert, A. Koutsioubas, S. Mattauch, T. Brückel, *Adv. Mater.* **2019**, *31*, 1806183.
[53] B. Cui, C. Song, G. Wang, Y. Yan, J. Peng, J. Miao, H. Mao, F. Li, C. Chen, F. Zeng, F. Pan, *Adv. Funct. Mater.* **2014**, *24*, 7233.
[54] T. Sato, G. Masuda, K. Takagi, *Electrochim. Acta* **2004**, *49*, 3603.
[55] T. Fujimoto, K. Awaga, *Phys. Chem. Chem. Phys.* **2013**, *15*, 8983.
[56] A. M. Perez-Muñoz, P. Schio, R. Poloni, A. Fernandez-Martinez, A. Rivera-Calzada, J. C. Cezar, E. Salas-Colera, G. R. Castro, J. Kinney, C. Leon, J. Santamaria, J. Garcia-Barriocanal, A. M. Goldman, *Proc. Natl. Acad. Sci. U. S. A.* **2017**, *114*, 215.
[57] M. Varela, M. P. Oxley, W. Luo, J. Tao, M. Watanabe, A. R. Lupini, S. T. Pantelides, S. J. Pennycook, *Phys. Rev. B* **2009**, *79*, 085117.
[58] A. Rozov, N. Burnashev, B. Sakmann, E. Neher, *J. Physiol.* **2001**, *531*, 807.
[59] R. S. Zucker, W. G. Regehr, *Annu. Rev. Physiol.* **2002**, *64*, 355.
[60] L. F. Abbott, S. B. Nelson, *Nat. Neurosci.* **2000**, *3*, 1178.
[61] D. Ielmini, Z. Wang, Y. Liu, *APL Mater.* **2021**, *9*, 050702.
[62] Y. Jeong, H. Lee, D. G. Ryu, S. H. Cho, G. Lee, S. Kim, S. Kim, Y. S. Lee, *Adv. Electron. Mater.* **2021**, *7*, 2100185.
[63] S. Yu, *Proc IEEE Inst Electr Electron Eng* **2018**, *106*, 260.

[64] Y. Choi, C. Lee, M. Kim, Y. Song, H. Hwang, D. Lee, in *IEEE Electron Device Letters*, **2019**, *40*, pp. 1992–1995.
[65] G. Bi, M. Poo, *J. Neurosci.* **1998**, *18*, 10464.
[66] C. Zamarreño-Ramos, L. A. Camuñas-Mesa, J. A. Pérez-Carrasco, T. Masquelier, T. Serrano-Gotarredona, B. Linares-Barranco, *Front. Neurosci.* **2011**, *5*, 26.
[67] H. Markram, J. Lübke, M. Frotscher, B. Sakmann, *Science* **1997**, *275*, 213.
[68] T. Masquelier, R. Guyonneau, S. J. Thorpe, *Neural Comput.* **2009**, *21*, 1259.
[69] Y. Nishitani, Y. Kaneko, M. Ueda, T. Morie, E. Fujii, *J. Appl. Phys.* **2012**, *111*, 124108.
[70] Y. Li, E. J. Fuller, J. D. Sugar, S. Yoo, D. S. Ashby, C. H. Bennett, R. D. Horton, M. S. Bartsch, M. J. Marinella, W. D. Lu, A. A. Talin, *Adv. Mater.* **2020**, *32*, 2003984.
[71] H. Boschker, J. Kautz, E. P. Houwman, W. Siemons, D. H. A. Blank, M. Huijben, G. Koster, A. Vailionis, G. Rijnders, *Phys. Rev. Lett.* **2012**, *109*, 157207.
[72] S. Ramanathan, *J. Vac. Sci. Technol., A* **2009**, *27*, 1126.
[73] T. Shiota, K. Sato, J. Cross, N. Wakiya, S. Tachikawa, A. Ohnishi, O. Sakurai, K. Shinoza, *Thin Solid Films* **2015**, *593*,1.
[74] N.-A. Nguyen, O. Schneegans, R. Salot, Y. Lamy, J. Giapintzakis, V. H. Mai, S. Oukassi, *Adv. Electron. Mater.* **2022**, *8*, 2200607.
[75] S. K. Chaluvadi, Z. Wang, L. M. C. deAraújo, P. Orgiani, V. Polewczyk, G. Vinai, O. Rousseau, V. Pierron, A. Pautrat, B. Domengès, D. G. Schlom, L. Méchin, *Appl. Surf. Sci.* **2022**, *579*, 152095.
[76] M. Romera, P. Talatchian, S. Tsunegi, F. A. Araujo, V. Cros, P. Bortolotti, K. Yakushiji, A. Fukushima, H. Kubota, S. Yuasa, D. Vodenicarevic, N. Locatelli, D. Querlioz, J. Grollier, *Nat. Commun.* **2022**, *13*, 883.